Optics Letters

Two-octave-wide (3–12 μm) subharmonic produced in a minimally dispersive optical parametric oscillator cavity

Q. Ru,[1] T. Kawamori,[1] P. G. Schunemann,[2] S. Vasilyev,[3] S. B. Mirov,[3,4] and K. L. Vodopyanov[1,*]

[1]CREOL, College of Optics and Photonics, University of Central Florida, Orlando, Florida 32816, USA
[2]BAE Systems, P.O. Box 868, MER15-1813, Nashua, New Hampshire 03061-0868, USA
[3]IPG Photonics-Mid-Infrared Lasers, Birmingham, Alabama 35203, USA
[4]Department of Physics, University of Alabama at Birmingham, Birmingham, Alabama 35294, USA
*Corresponding author: vodopyanov@creol.ucf.edu

Received 27 July 2020; revised 7 December 2020; accepted 8 December 2020; posted 7 January 2021 (Doc. ID 403910); published 3 February 2021

We report a subharmonic (frequency-divide-by-2) optical parametric oscillator (OPO) with a continuous wavelength span of 3 to 12 μm (−37 dB level) that covers most of the molecular rovibrational "signature" region. The key to obtaining such a wide spectral span is the use of an OPO with a minimal dispersion—through the choice of intracavity elements, the use of all gold-coated mirrors, and a special "injector" mirror. The system delivers up to 245 mW of the average power with the conversion efficiency exceeding 20% from a 2.35 μm Kerr-lens mode-locked pump laser.

https://doi.org/10.1364/OL.403910

Broadband coherent emitters in the mid-infrared (MIR) region are powerful photonic tools that can be used for massively parallel, rapid, and precise spectroscopic measurements [1–3]. A variety of approaches to generate more-than-octave-wide spectral outputs across the MIR (>3 μm) include supercontinuum generation in highly nonlinear fibers [4–13], waveguides [14,15], and bulk media [16–20], and intrapulse difference-frequency generation in quadratic media [21–25].

Subharmonic optical parametric oscillators (OPOs) are a special class of noteworthy broadband MIR sources [26–28] now widely used in dual-frequency-comb spectroscopic studies [29], random number generators [30], and coherent Ising machines [31]. A subharmonic OPO is a coherent frequency divider without any excess phase noise that rigorously both downconverts and augments the spectrum of the pump laser [32–34]. Its main benefits are low (10 mW level) oscillation threshold, broad bandwidth, and excellent stability when actively locked for operation at subharmonic. Yet another advantage is high conversion efficiency from the pump laser that can be as high as 64% [35].

Here we report on producing an optical subharmonic with an unprecedentedly broadband output that covers a MIR range of 3–12 μm with high, 245 mW, average output power. Such a broad spectrum was enabled by an unconventional long-wave pump and careful optimization of the cavity dispersion.

The pump source (Fig. 1) was a Kerr-lens mode-locked Cr^{2+}:ZnS oscillator with 2.35 μm central wavelength, 1.2 W average power, 79 MHz repetition frequency, and bandwidth-limited pulse duration of 62 fs. The bowtie ring OPO cavity was composed of gold-coated mirrors only. Two of them (M_2 and M_3) were parabolic with an off-axis angle of 30° and 30 mm apex radius of curvature (effective focal distance 16 mm). The other two mirrors were flat (not shown are two pairs of folding mirrors used to reduce the footprint). To incouple the pump laser beam, we used an intracavity pump injector—a dielectric mirror deposited on a thin (0.5 mm) wedged (0.5°) ZnSe substrate. The coating on one side had high reflection (>90%) for the 2.35 μm pump and high transmission for the OPO signal plus idler waves (>90% at 3.5–7 μm and >50% at 2.8–12 μm); the other side was antireflection coated for 3–12 μm. An uncoated ZnSe "tuning" wedge (0.3–0.8 mm thick, 1° angle) inside the cavity was used to (i) fine tune the intracavity GDD

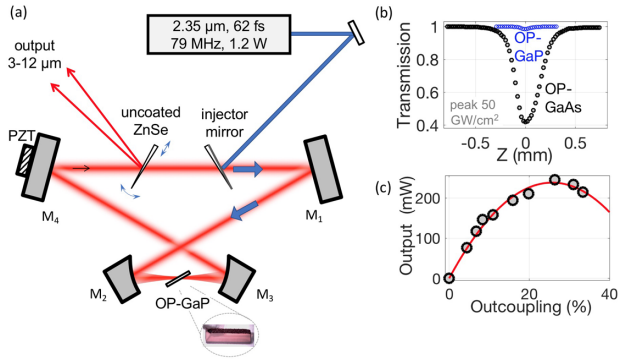

Fig. 1. (a) Schematic of the subharmonic OPO. $M_1 - M_4$, gold-coated mirrors; PZT, piezoelectric transducer. (b) Z-scan curves for the OP-GaP and OP-GaAs measured at $\lambda = 2.35$ μm. (c) OPO output power versus outcoupling strength. The solid curve is a trace for the eye.

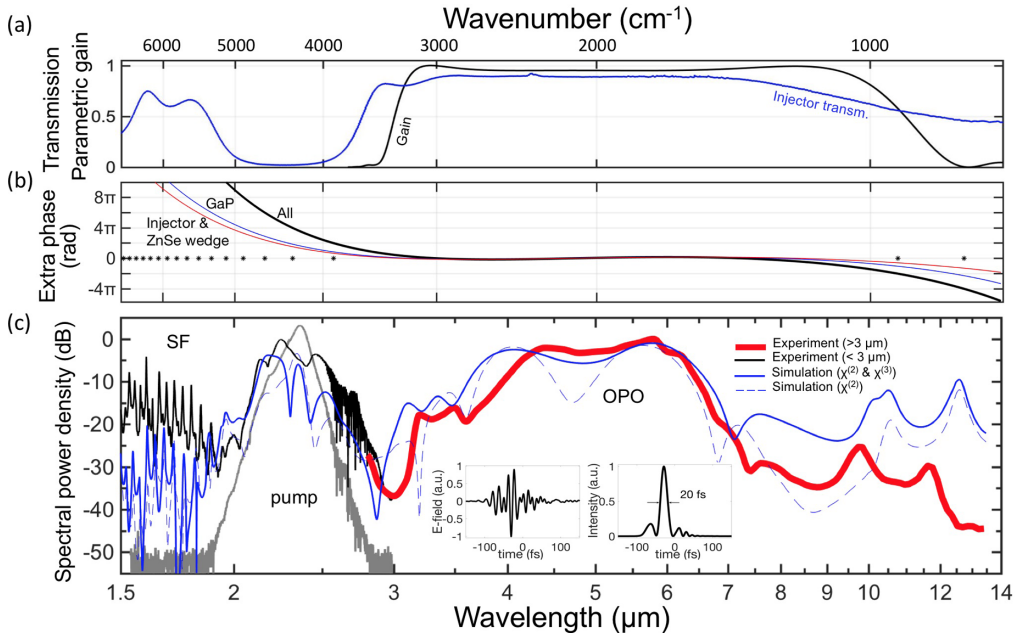

Fig. 2. (a) Normalized parametric gain and injector transmission versus wavelength (both wavelength and frequency are on a log scale). (b) Extra phase per cavity round trip (black curve) and contribution of separate elements: OP-GaP (blue) and injector plus tuning wedge combined (red). The asterisks indicate spectral points where the extra phase reaches multiples of 2π. (c) Overall spectrum that includes that of the OPO (red), and the spectrum of the pump and SF (black). The incoming "cold" pump spectrum is in gray. The simulated spectrum is shown in blue (solid line, with both $\chi^{(2)}$ and $\chi^{(3)}$ included; dashed line, with only $\chi^{(2)}$). The ripples near 2.7 μm are due to water absorption in the air. Inset, simulated time-domain profiles for the electric field and intensity of the OPO ($\lambda > 3$ μm) pulse.

and (ii) vary the OPO outcoupling via Fresnel reflection. Both the injector and the outcoupling wedge introduced a minimal group delay dispersion (GDD), mostly coming from the bulk of ZnSe, whose group velocity dispersion (GVD) is small within the OPO span (ZnSe has zero GVD crossing at 4.81 μm). A broad bandwidth parametric gain was provided by a 0.5-mm-long orientation-patterned gallium phosphide (OP-GaP)—a quasi-phase-matched (QPM) crystal with wide transparency range of 0.55–13 μm [36] and a large second-order nonlinear coefficient $d_{14} = 35$ pm/V [37]. The crystal had a QPM period of 110 μm and was placed at Brewster's angle (71°) with all the interacting waves co-polarized along ⟨111⟩ direction. With its zero GVD at $\lambda \approx 4.8$ μm, the OP-GaP introduced a minimal GDD inside the cavity. Figure 2(a) plots the wavelength dependence of the OP-GaP parametric gain and the injector transmission, while Fig. 2(b) shows a computed extra phase per round trip due to cavity GDD; also shown are contributions from individual cavity elements.

First, we characterized the nonlinear OP-GaP loss at our 2.35 μm pump intensities via the Z-scan and compared OP-GaP with orientation-patterned gallium arsenide (OP-GaAs), another notable QPM nonlinear material [28]. Figure 1(b) compares Z-scan curves for these two crystals (both 0.5-mm-long and placed at Brewster's angle) at the peak on-axis intensity (inside the crystals) of ≈50 GW/cm^2. While we observed a large (60%) transmission dip in the OP-GaAs, due to three-photon absorption (3PA), in good accordance with its known 3PA coefficient [38], there was only a small, 1.5% dip in the OP-GaP. This result can be explained by the larger bandgap of GaP (direct 2.78 eV, indirect 2.26 eV), as compared to that of GaAs (1.42 eV), and proves that OP-GaP is better suited for the 2.35 μm pump at the above irradiances.

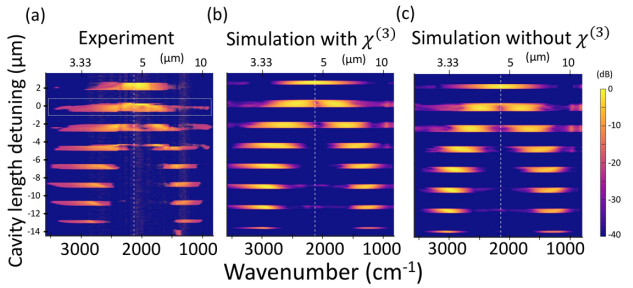

Fig. 3. 2D color intensity plots of the OPO spectra as the resonator length is detuned. (a) Experimental spectrum. (b) Simulated spectrum with both $\chi^{(2)}$ and $\chi^{(3)}$ included. (c) Simulated spectrum with only $\chi^{(2)}$ included. The top stripes correspond to the subharmonic regime, while the lower ones correspond to the non-degenerate regime with distinct signal and idler bands.

Figure 3(a) shows 2D color coded plots of the OPO spectra as the resonator length is detuned [we used a grating monochromator and a mercury cadmium telluride (MCT) detector with 12 μm infrared cutoff]. Since the OPO is doubly resonant, it only oscillates within discrete bands, in terms of the round trip path length, separated by approximately the pump wavelength [28].

The OPO operated in the "ramp" mode—a piezo actuator attached to one of the mirrors tuned the cavity length sequentially through several resonances. Figure 3(b) presents a simulation including both $\chi^{(2)}$ and $\chi^{(3)}$ interactions in the

OP-GaP, while Fig. 3(c) is a simulation accounting for only $\chi^{(2)}$ processes (including cascaded ones; see Supplement 1).

Subsequently, the OPO cavity length was actively locked to a resonance that produced the broadest spectrum [the second stripe from the top in Fig. 3(a)]. By tuning GDD via adjusting the ZnSe tuning wedge's thickness, we achieved the broadest spectrum spanning 3–12 μm at −37 dB level [Fig. 2(c)]. We also analyzed the spectrum in the near-IR by coupling the output to an optical spectrum analyzer (Yokogawa AQ6376 for the 1.5–3 μm and Agilent 86142B for the 1–1.5 μm range). When the OPO is operational, the pump spectrum [Fig. 2(c), black curve] broadens with respect to its initial shape (gray curve)—a result of the frequency backconversion. The output at $\lambda < 2$ μm is due to the parasitic sum-frequency (SF) generation in the OP-GaP, between the pump and the OPO waves. SF is partially resonant in the cavity, but has a mismatched round trip group delay as compared to the pump laser repetition period, which causes spectral modulation with the maxima observed when the extra phase acquires multiples of 2π [these points (calculation) are indicated by asterisks in Fig. 2(b)]. For the same reason, the peaks at 9.8 μm and 11.8 μm in the OPO spectrum correspond to the extra phase of 2π and 4π, respectively). The simulated spectrum in Fig. 2(c) (blue curve) explains these phenomena well. (The mismatch between experiment and theory at >10 μm can be explained by the declining sensitivity of MCT detector near its cutoff.)

It appears that, in addition to $\chi^{(2)}$, the cubic nonlinearity $\chi^{(3)}$ in the OP-GaP crystal contributes to the OPO spectrum. In fact, because of the high nonlinear index in GaP (an estimated MIR value $n_2 = 1.9 \times 10^{-18}$ m^2/W; see Supplement 1) and high circulating OPO peak intensity, $I_{\max} \sim 100$ GW/cm^2 inside the OP-GaP, the dynamic phase shift can be estimated to be $\Delta\varphi = \frac{2\pi}{\lambda} n_2 I_{\max} l \approx 1.3$ rad (here $\lambda \approx 4.7$ μm is the center OPO wavelength, and l is the length of the OP-GaP crystal), which may induce a noticeable self-phase modulation (SPM). For example, when the OPO is operating in a non-degenerate mode [bottom stripes in Fig. 3(a)], one can see that the stripes corresponding to the signal wave (blue side of the spectrum) are broader than those for the idler wave. For a three-photon process alone, the widths of the stripes (in frequency units) should be identical because the photons are created in pairs and their frequencies are equally spaced from the degeneracy point. The observed asymmetry can be attributed to the spectral broadening induced by self- and cross-phase modulation, which is proportional to the center frequency and thus is larger for the signal wave. The simulated spectra of Figs. 3(b) and 3(c) support this idea—the asymmetry of the non-degenerate spectrum appears only when $\chi^{(3)}$ effects are turned on. Yet, another $\chi^{(3)}$ effect—four wave mixing (FWM) may contribute to the expanding and smoothening of the long-wave portion of the OPO spectrum. In fact, for the degenerate FWM process $2\omega_1 = \omega_3 + \omega_4$, the phase-matching condition $2k_1 = k_3 + k_4 + 2\gamma P$ [39] can be satisfied in the OP-GaP (here ω_i are angular frequencies, k_i are wave vector modules, $\gamma = n_2\omega/cA_{\text{eff}}$ is the nonlinear FWM parameter, c is the speed of light, A_{eff} is an effective beam area, and P is the peak power of the beam at ω_1). One example is the energy transfer from the 6 μm to the weaker 11 μm portion of the spectrum with $\omega_1 = 2\pi c/(6\ \mu\text{m})$, $\omega_3 = 2\pi c/(11\ \mu\text{m})$, and $\omega_4 = 2\pi c/(4.5\ \mu\text{m})$, where the phase-matching is satisfied due to a weakly anomalous dispersion of GaP at >4.8 μm. These effects are included in our simulations (see Supplement 1). Looking at the simulated plot of Fig. 2(c) with both $\chi^{(2)}$ and $\chi^{(3)}$, and only $\chi^{(2)}$ included, it can be observed that the main effect of $\chi^{(3)}$ is to amplify to the spectrum between 7 and 11 μm and smooth the spectrum around 4.7 μm due to SPM.

To verify that the subharmonic OPO output is a single (free-running) comb and its spectral components share a common carrier-envelope offset (CEO) frequency, we performed radio-frequency beatnote measurements in different parts of the spectrum. We observed $f-$ to $-2f$ beatnotes between the 3.5 μm and frequency-doubled 7 μm portions of the OPO spectrum, as well as beatnotes between the overlapping second harmonic of the pump and SF spectra at 1.3 μm, with both experiments confirming the mutual coherence between the OPO and the pump (see Supplement 1).

We optimized the OPO performance by measuring the output power as a function of the outcoupling (by varying the angle of the ZnSe outcoupling wedge) [Fig. 1(c)]. The average output power (shared about equally between the two reflections from the tuning wedge) reached 245 mW at the outcoupling strength of 26% (two wedge surfaces combined). The OPO pump threshold was 55 mW for 3.4% and approximately 250 mW for 26% outcoupling. In most of our experiments, the typical pump depletion was as high as 83%. The OPO spectra looked similar at different outcouplings; however, a high dynamic range spectrum of Fig. 2(c) was taken at 3.4% outcoupling (at the average output power of 50 mW).

In conclusion, we achieved a broadband, 3–12 μm, output from a subharmonic OPO with the average power up to 245 mW and optical conversion efficiency exceeding 20%. The instantaneous MIR bandwidth is the widest for subharmonic OPOs. The key to getting such a broad spectrum was the use of a long-wave 2.35 μm pump and a minimally dispersive cavity with (i) all-gold-coated mirrors, (ii) a pump injector, and (iii) optically thin intracavity elements (including the OP-GaP gain crystal) with zero GVD crossings near the OPO spectral midpoint. In addition to quadratic, cubic nonlinear effects in the OP-GaP contribute to broadening the spectrum, with both of these processes preserving the OPO temporal coherence. Since the OPO was pumped by a free-running femtosecond oscillator, its output was also a free-running frequency comb. A CEO-stabilized Cr:ZnS comb has been reported most recently [40]; thanks to the intrinsic coherence of a subharmonic OPO to the pump, this opens up the possibility of a fully stabilized MIR comb linked to a primary frequency standard. Lastly, thanks to low pump power requirements, a compact broadband dual-comb spectroscopic system driven by a pair of phase-locked Cr:ZnS oscillators can be used in a plethora of spectroscopic and metrological applications.

Funding. Office of Naval Research (N00014-15-1-2659, N00014-18-1-2176); Defense Advanced Research Projects Agency (W31P4Q-15-1-0008).

Disclosures. The authors declare no conflicts of interest.

Supplemental documents. See Supplement 1 for supporting content.

REFERENCES

1. A. Schliesser, N. Picqué, and T. W. Hänsch, Nat. Photonics **6**, 440 (2012).
2. N. Picqué and T. W. Hänsch, Nat. Photonics **13**, 146 (2019).

3. Z. E. Loparo, E. Ninnemann, Q. Ru, K. L. Vodopyanov, and S. S. Vasu, Opt. Lett. **45**, 491 (2020).
4. G. Qin, X. Yan, C. Kito, M. Liao, C. Chaudhari, T. Suzuki, and Y. Ohishia, Appl. Phys. Lett. **95**, 161103 (2009).
5. Y. Yu, B. Zhang, X. Gai, C. Zhai, S. Qi, W. Guo, Z. Yang, R. Wang, D.-Y. Choi, S. Madden, and B. Luther-Davies, Opt. Lett. **40**, 1081 (2015).
6. U. Møller, Y. Yu, I. Kubat, C. R. Petersen, X. Gai, L. Brilland, D. Méchin, C. Caillaud, J. Troles, B. Luther-Davies, and O. Bang, Opt. Express **23**, 3282 (2015).
7. D. D. Hudson, M. Baudisch, D. Werdehausen, B. J. Eggleton, and J. Biegert, Opt. Lett. **39**, 5752 (2014).
8. L.-R. Robichaud, V. Fortin, J.-C. Gauthier, S. Châtigny, J.-F. Couillard, J.-L. Delarosbil, R. Vallée, and M. Bernier, Opt. Lett. **41**, 4605 (2016).
9. C. R. Petersen, U. Møller, I. Kubat, B. Zhou, S. Dupont, J. Ramsay, T. Benson, S. Sujecki, N. Abdel-Moneim, Z. Tang, D. Furniss, A. Seddon, and O. Bang, Nat. Photonics **8**, 830 (2014).
10. D. D. Hudson, S. Antipov, L. Li, I. Alamgir, T. Hu, M. El Amraoui, Y. Messaddeq, M. Rochette, S. D. Jackson, and A. Fuerbach, Optica **4**, 1163 (2017).
11. T. Cheng, K. Nagasaka, T. H. Tuan, X. Xue, M. Matsumoto, H. Tezuka, T. Suzuki, and Y. Ohishi, Opt. Lett. **41**, 2117 (2016).
12. Z. Zhao, B. Wu, X. Wang, Z. Pan, Z. Liu, P. Zhang, X. Shen, Q. Nie, S. Dai, and R. Wang, Laser Photon. Rev. **11**, 1700005 (2017).
13. N. Nagl, K. F. Mak, Q. Wang, V. Pervak, F. Krausz, and O. Pronin, Opt. Lett. **44**, 2390 (2019).
14. Y. Yu, X. Gai, P. Ma, D. Y. Choi, Z. Y. Yang, R. P. Wang, S. Debbarma, S. J. Madden, and B. Luther-Davies, Laser Photon. Rev. **8**, 792 (2014).
15. N. Singh, D. D. Hudson, Y. Yu, C. Grillet, S. D. Jackson, A. Casas-Bedoya, A. Read, P. Atanackovic, S. G. Duvall, S. Palomba, B. Luther-Davies, S. Madden, D. J. Moss, and B. J. Eggleton, Optica **2**, 797 (2015).
16. Y. Yu, X. Gai, T. Wang, P. Ma, R. Wang, Z. Yang, D.-Y. Choi, S. Madden, and B. Luther-Davies, Opt. Mater. Express **3**, 1075 (2013).
17. M. Liao, W. Gao, T. Cheng, X. Xue, Z. Duan, D. Deng, H. Kawashima, T. Suzuki, and Y. Ohishi, Appl. Phys. Express **6**, 032503 (2013).
18. O. Mouawad, P. Béjot, F. Billard, P. Mathey, B. Kibler, F. Désévédavy, G. Gadret, J.-C. Jules, O. Faucher, and F. Smektala, Opt. Mater. **60**, 355 (2016).
19. S. Ashihara and Y. Kawahara, Opt. Lett. **34**, 3839 (2009).
20. J. J. Pigeon, S. Y. Tochitsky, C. Gong, and C. Joshi, Opt. Lett. **39**, 3246 (2014).
21. I. Pupeza, D. Sánchez, J. Zhang, N. Lilienfein, M. Seidel, N. Karpowicz, T. Paasch-Colberg, I. Znakovskaya, M. Pescher, W. Schweinberger, V. Pervak, E. Fill, O. Pronin, Z. Wei, F. Krausz, A. Apolonski, and J. Biegert, Nat. Photonics **9**, 721 (2015).
22. J. Zhang, K. Fritsch, Q. Wang, F. Krausz, K. F. Mak, and O. Pronin, Opt. Lett. **44**, 2986 (2019).
23. S. Vasilyev, I. S. Moskalev, V. O. Smolski, J. M. Peppers, M. Mirov, A. V. Muraviev, K. Zawilski, P. G. Schunemann, S. B. Mirov, K. L. Vodopyanov, and V. P. Gapontsev, Optica **6**, 111 (2019).
24. S. Vasilyev, V. Smolski, I. Moskalev, J. Peppers, M. Mirov, Y. Barnakov, V. Fedorov, D. Martyshkin, A. Muraviev, K. Zawilski, P. Schunemann, S. Mirov, K. Vodopyanov, and V. Gapontsev, Proc. SPIE **11264**, 1126407 (2020).
25. A. S. Kowligy, H. Timmers, A. J. Lind, U. Elu, F. C. Cruz, P. G. Schunemann, J. Biegert, and S. A. Diddams, Sci. Adv. **5**, eaaw8794 (2019).
26. N. Leindecker, A. Marandi, R. L. Byer, and K. L. Vodopyanov, Opt. Express **19**, 6296 (2011).
27. V. O. Smolski, H. Yang, S. D. Gorelov, P. G. Schunemann, and K. L. Vodopyanov, Opt. Lett. **41**, 1388 (2016).
28. V. Smolski, S. Vasilyev, I. Moskalev, M. Mirov, Q. Ru, A. Muraviev, P. Schunemann, S. Mirov, V. Gapontsev, and K. Vodopyanov, Appl. Phys. B **124**, 101 (2018).
29. A. V. Muraviev, V. O. Smolski, Z. E. Loparo, and K. L. Vodopyanov, Nat. Photonics **12**, 209 (2018).
30. A. Marandi, N. C. Leindecker, K. L. Vodopyanov, and R. L. Byer, Opt. Express **20**, 19322 (2012).
31. A. Marandi, Z. Wang, K. Takata, R. L. Byer, and Y. Yamamoto, Nat. Photonics **8**, 937 (2014).
32. A. Marandi, N. Leindecker, V. Pervak, R. L. Byer, and K. L. Vodopyanov, Opt. Express **20**, 7255 (2012).
33. K. F. Lee, N. Granzow, M. A. Schmidt, W. Chang, L. Wang, Q. Coulombier, J. Troles, N. Leindecker, K. L. Vodopyanov, P. G. Schunemann, M. E. Fermann, P. St.J. Russell, and I. Hartl, Opt. Lett. **39**, 2056 (2014).
34. C. Wan, P. Li, A. Ruehl, and I. Hartl, Opt. Lett. **43**, 1059 (2018).
35. A. Marandi, K. A. Ingold, M. Jankowski, and R. L. Byer, Optica **3**, 324 (2016).
36. L. Maidment, O. Kara, P. G. Schunemann, J. Piper, K. McEwan, and D. T. Reid, Appl. Phys. B **124**, 143 (2018).
37. K. L. Vodopyanov, *Laser-Based Mid-Infrared Sources and Applications* (Wiley, 2020).
38. W. C. Hurlbut, Y.-S. Lee, K. L. Vodopyanov, P. S. Kuo, and M. M. Fejer, Opt. Lett. **32**, 668 (2007).
39. G. Agrawal, *Nonlinear Fiber Optics, Optics and Photonics* (Elsevier Science, 2012).
40. S. Vasilyev, V. Smolski, J. Peppers, I. Moskalev, M. Mirov, Y. Barnakov, S. Mirov, and V. Gapontsev, Opt. Express. **27**, 35079 (2019).